RSC Advances

PAPER

View Article Online
View Journal | View Issue



Cite this: *RSC Adv.*, 2023, **13**, 17324

# Enhanced photocatalytic activity of modified black phosphorus-incorporated PANi/PAN nanofibers†

Shadi Asgari,[a] Ghodsi Mohammadi Ziarani,*[a] Alireza Badiei,*[b] Rajender S. Varma,[c] Siavash Iravani[d] and Fatemeh Mohajer[a]

Enhancement of the photocatalytic activity of black phosphorus (BP) is a highly challenging proposition. The fabrication of electrospun composite nanofibers (NFs) through the incorporation of modified BP nanosheets (BPNs) into conductive polymeric NFs has been recently introduced as a newer strategy not only to enhance the photocatalytic activity of BPNs but also to overcome their drawbacks including ambient instability, aggregation, and hard recycling, which exist in their nanoscale powdered forms. The proposed composite NFs were prepared through the incorporation of silver (Ag)-modified BPNs, gold (Au)-modified BPNs, and graphene oxide (GO)-modified BPNs into polyaniline/polyacrylonitrile (PANi/PAN) NFs by an electrospinning process. The successful preparation of the modified BPNs and electrospun NFs was confirmed by the characterization techniques of Fourier-transform infrared spectroscopy (FT-IR), ultraviolet-visible (UV-vis), powder X-ray diffraction (PXRD), and Raman spectroscopy. The pure PANi/PAN NFs exhibited high thermal stability with a main weight loss of ~23% for the temperature range of 390–500 °C, and the thermal stability of NFs was enhanced after their incorporation with the modified BPNs. The BPNs@GO-incorporated PANi/PAN NFs indicated improved mechanical properties compared to the pure PANi/PAN NFs with tensile strength (TS) of 1.83 MPa and elongation at break (EAB) of 24.91%. The wettability of the composite NFs was measured in the range of 35–36°, which exhibited their good hydrophilicity. The photodegradation performance was found in the sequence of BPNs@GO > BPNs@Au > BPNs@Ag > bulk BP ~BPNs > red phosphorus (RP) for methyl orange (MO) and in the sequence of BPNs@GO > BPNs@Ag > BPNs@Au > bulk BP > BPNs > RP for methylene blue (MB), accordingly. The composite NFs degraded the MO and MB dyes more efficiently relative to the modified BPNs and pure PANi/PAN NFs.

Received 16th March 2023
Accepted 29th May 2023

DOI: 10.1039/d3ra01744c

rsc.li/rsc-advances



## 1. Introduction

Finding an effective method to increase the photocatalytic activity of black phosphorus (BP) is immensely challenging. The incorporation of modified BP into conductive polymeric nanofibers (NFs) has recently been introduced as a new strategy not only to enhance the photocatalytic activity of BP but also to overcome the drawbacks of aggregation and ambient instability of BP. BP is a layered two-dimensional (2D) photocatalyst with visible near-infrared activity, layer-dependent bandgap, high carrier mobility, excellent mechanical resistance, biocompatibility and biodegradability, and high photothermal conversion efficiency.[1–6] However, the lone pair electrons on the phosphorus atoms of BP can react with oxygen and water molecules, which leads to diminishing the photocatalytic activity and ambient stability of BP.[7–9] Surface modification techniques such as covalent or non-covalent functionalizations, and metal-ion modification are common methods devoted to augmenting the ambient stability and photocatalytic activity of BP.[10–21] The incorporation of BP into conductive polymeric matrices is another method recently introduced for enhancing the photocatalytic activity.[22–24]

In the metal-ion modification, plasmonic noble metals such as gold (Au) and silver (Ag) are utilized for the modification of BP. They display strong light absorption through excitation of a localized surface plasmon resonance, along with the properties of strong light absorption, vigorous nature, recyclability, and high surface areas, which render the noble metals as good photocatalytic materials.[25–28] The noble metals can also passivate BP by chemical adsorption through making cation–π interactions. Indeed, BP acts as a reducing agent by losing its electrons and

[a]*Department of Organic Chemistry, Faculty of Chemistry, Alzahra University, P.O. Box 1993893973, Tehran, Iran. E-mail: gmohammadi@alzahra.ac.ir*

[b]*School of Chemistry, College of Science, University of Tehran, Tehran, Iran. E-mail: abadiei@ut.ac.ir*

[c]*Regional Centre of Advanced Technologies and Materials, Czech Advanced Technology and Research Institute, Palacký University in Olomouc, Šlechtitelů 27, 783 71 Olomouc, Czech Republic*

[d]*Faculty of Pharmacy and Pharmaceutical Sciences, Isfahan University of Medical Sciences, Isfahan, Iran*

† Electronic supplementary information (ESI) available. See DOI: https://doi.org/10.1039/d3ra01744c

binding to the surface of metal ions.[15,29] In addition, BP can form a moderate chemical bond with metal atoms that exhibit high adsorption energy and low distortion ability, facilitating the higher stability of BP/metal ion hybrids. The stable metal–P covalent bonds are formed between BPNs and metal ions that cause the contact of oxygen only with the surface of BPNs loaded with the metal nanoparticles (NPs), thus reducing the rate of BPNs oxidation.[30] BP nanosheets (BPNs) have also been deployed as solid support to control the size, coverage, and chemical state of surface-anchored metal NPs.[31] The most common examples are Ag and Au-modified BPNs, termed as BPN@Ag and BPN@Au complexes, which exploit the precursors of tetrachloroauric acid ($HAuCl_4$) and silver nitrate ($AgNO_3$), respectively, with no additional reducing agents.[16,29,30,32,33] BP can also partially reduce oxygen-containing functional groups of graphene oxide (GO) and produce covalent bonds with it or can be distributed on the surface of GO nanosheets.[30,34,35] GO shows great photogenerated electron–hole carrier mobility and low recombination that increases photocatalytic activity.[36–38] The presence of GO also lessens the degradation rate of BPNs and reduces their oxidation by forming P–C and P–O–C covalent bonds.[30] Thus, it is expected that modifying BPNs with Ag/Au metals and GO enhances both, the photocatalytic activity and ambient stability of BPNs.

The incorporation of BP into conductive polymeric nanofibers (NFs) is another strategy developed recently to fabricate the stabilized BP/polymer composite NFs with enhanced photocatalytic activity. Indeed, the conductive polymers offer a broad light absorption region and high electron mobility leading to great conductivity and increased photocatalytic activity.[39–44] These polymers protect BP from oxygen and water by serving as efficient light barriers for BP to prevent photooxidation owing to donor–acceptor interactions between BP and themselves.[39,40] PANi, poly(3,4-ethylenedioxythiophene), polyacetylene, polyfuran, poly(*p*-phenylenevinylene), polythiophene, and their derivatives are some of the common types of conductive polymers.[45–47] Unfortunately, the spinning solution of conductive polymers does not have sufficient viscosity for the successful fabrication of NFs, thus necessitating the addition of an auxiliary polymer such as polyacrylonitrile (PAN). The PAN/PANi NFs serve as an electrocatalytically active matrix to prevent BPNs from agglomerations as well as to enhance their photocatalytic performance.[48] Besides, PAN-based NFs have the advantages of (1) low density leading to their floating on the water surface that promotes easy separation and recycling and light penetration, and (2) high porosity and specific surface area that enhances the photocatalytic activity by providing the remarkable contact between photocatalysts and pollutants.[49–52] The incorporation of the powdered form of photocatalysts into the electrospun NFs is also a new strategy not only to enhance the photocatalytic activity but also to overcome the drawbacks of the photocatalytic powdered forms namely aggregation, photocorrosion, and hard recycling and separation.[53,54] Notably, the electrospun NFs have a high specific surface area and ultrathin thickness, offering many active sites leading to a decrease in the recombination of electron–hole carriers.[55,56]

Herein, the modified BPNs-incorporated PANi/PAN NFs (electrospun composite NFs) have been prepared with enhanced photocatalytic activity through the modification of BPNs with Ag/Au metals and GO and their incorporation into PANi/PAN NFs *via* an electrospinning process. The photocatalytic activity of BPNs before and after the surface modification was investigated by photodegradation studies deploying cationic and anionic organic dyes. A comparative photodegradation study of the dyes outperformed among the modified BPNs in the powdered forms and their corresponding electrospun composite NFs.

## 2. Experimental section

Chemicals and instruments are provided in the ESI.† The synthesis procedures of bulk BP, BPNs, BPNs@Ag, BPNs@Au, and BPNs@GO and the fabrication procedure of electrospun composite NFs are described below.

### 2.1. Preparation of bulk black phosphorus (bulk BP)

BP was prepared through the solvothermal method by using ethylenediamine and red phosphorus (RP) as reported by Zhu *et al.*[57] and Ozawa *et al.*[58] A dispersion of RP (1.8 g) in ethylenediamine (120 mL) was prepared, transferred into a Teflon-lined stainless autoclave, and heated at 170 °C for 24 h. The BP product was cooled fast, washed with ethanol, and collected by centrifuge. The vacuum-dried BP was preserved in a sealed tube to prevent oxidation.

### 2.2. Preparation of BP nanosheets (BPNs)

BPNs were synthesized by liquid phase exfoliation of bulk BP with the use of DMF as an exfoliation solvent.[59] The bulk BP (0.15 g) was ground in a mortar containing DMF (6 mL). 2 mL of supernatant was picked up and 2 mL of fresh DMF was added into the residual mixture and ground additionally. The process was performed several times. After purging argon into the mixture and its sealing, it was sonicated in an ice bath by a probe ultrasonicator for 4 h. The BPNs were centrifuged at 8000 rpm for 6 min.

### 2.3. Preparation of silver modified BPNs (BPNs@Ag) and gold modified BPNs (BPNs@Au)

BPNs were used as green reductants due to their lone pair electrons existing on the phosphorus atoms. The BPNs (0.02 g) were homogeneously dispersed in deionized water (DI water, 1.5 mL) and an aqueous solution of $AgNO_3$ (1 mg $mL^{-1}$, 5 mL) was added dropwise to the mixture and stirred for 24 h to obtain BPN@Ag. To prepare BPN@Au, an aqueous solution of $HAuCl_4$ (1 mg $mL^{-1}$, 5 mL) and a stirring time of 24 h were used. The BPN@Ag and BPN@Au products were collected by deploying a centrifuge at 11 000 rpm for 10 min.

### 2.4. Preparation of graphene oxide modified BPNs (BPNs@GO)

BPNs can reduce the oxygen-containing functional groups of GO and form covalent bonding of P–O–C and P–C.[34] A dispersion of BPNs (0.03 g) in DMF (30 mL) was placed in an ice bath and the as-prepared GO (0.02 g)[60] was added to the mixture. The

mixture was sonicated for 3 h with working for 5 s and intervals of 2 s. The BPN@GO product was collected with a centrifuge at 11 000 rpm for 10 min.

### 2.5. Fabrication of electrospun NFs

The electrospun PAN NFs (8.0 wt%) and PANi/PAN NFs were fabricated *via* electrospinning the spinning solution of PAN (0.5 g) in DMF (6 mL) and a mixture of PANi (0.125 g) and PAN (0.5 g) (1 : 4 wt ratio) in DMF (6 mL), respectively. For the fabrication of composite NFs including RP-loaded PANi/PAN NFs, bulk BP-loaded PANi/PAN NFs, BPNs-loaded PANi/PAN NFs, BPNs@Ag-loaded PANi/PAN NFs, BPNs@Au-loaded PANi/PAN NFs, and BPNs@GO-loaded PANi/PAN NFs, the spinning solutions were first prepared by dispersing RP, bulk BP, BPNs, BPNs@Ag, BPNs@Au, or BPNs@GO (0.015 g) in DMF (1 mL) and mixing them with PANi/PAN polymeric mixture (0.125 g PANi and 0.5 g PAN in 5 mL DMF) and then electrospinning under the conditions of 19 kV, needle tip to the collector distance of 13 cm, the needle diameter of 21-gauge, and feeding rate of 1.0 mL $h^{-1}$. The ensued NFs collected over the aluminum foil were peeled off and dried at room temperature. Fig. 1 presents the synthesis procedures for bulk BP, BPNs, BPNs@Ag, BPNs@Au, and BPNs@GO and the fabrication of electrospun composite NFs.

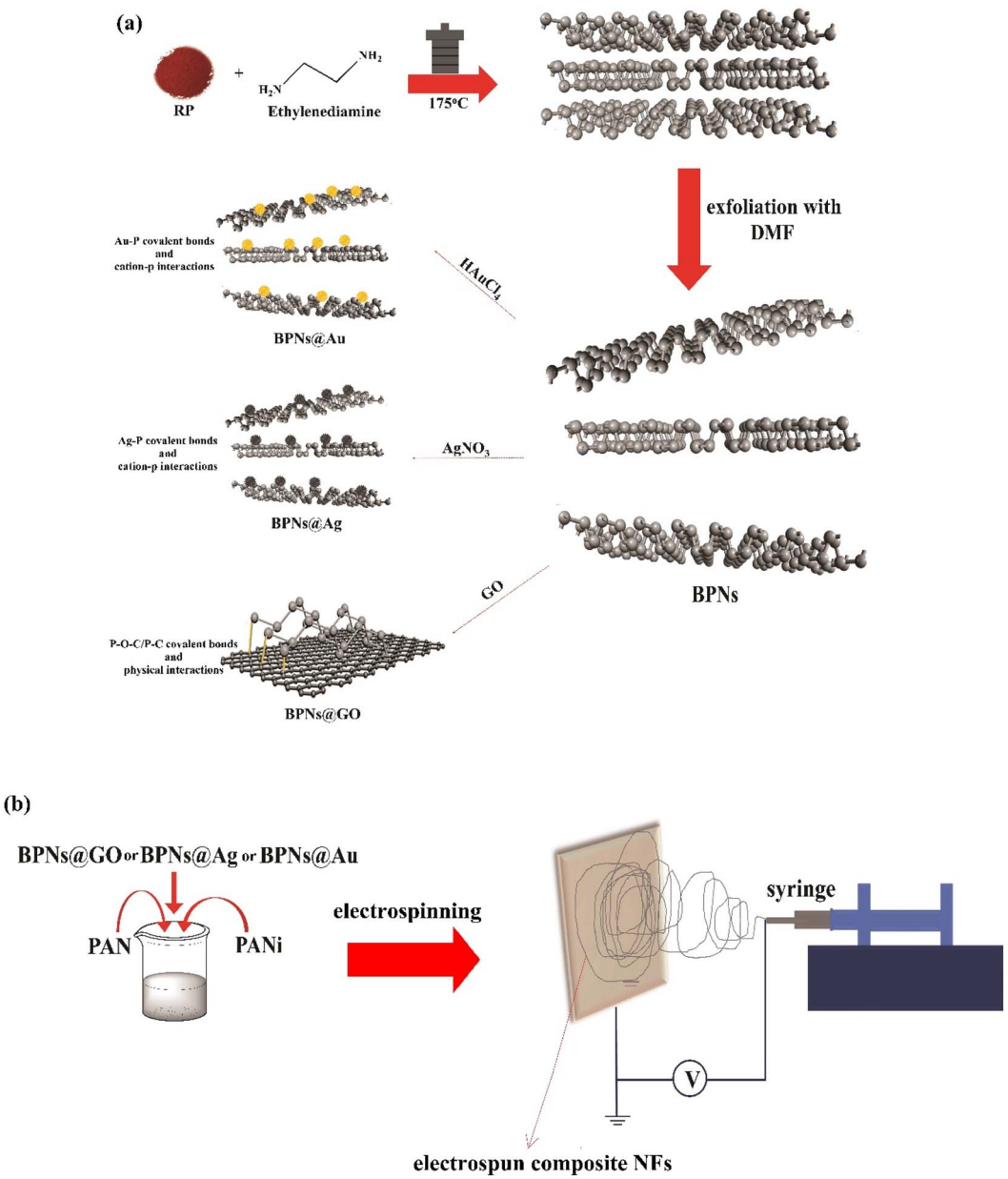


Fig. 1 The synthesis procedures of bulk BP, BPNs, BPNs@Ag, BPNs@Au, and BPNs@GO (a), and the fabrication procedure of electrospun composite NFs (b).

### 2.6. Tensile test

The mechanical properties of the electrospun NFs were investigated by a tensile test machine. A crosshead speed of 1 mm $min^{-1}$ was used to record the tensile curves of the electrospun NFs. The NFs in a rectangular shape and dimensions of 60 mm × 10 mm ($L \times W$) with a gauge length of 40 mm were prepared. The thickness of NFs obtained in the range of 0.060–0.099 mm with a digital micrometer. The stress–strain curves were drawn using the following equations:

$$\sigma = \left(\frac{f}{w \times h}\right)$$

$$\varepsilon(\%) = \left(\frac{l - l_0}{l_0}\right) \times 100$$

$f$ is breaking force, $w$ is width of nanofiber, $h$ is thickness of nanofiber, $l$ is breaking length, and $l_0$ is gauge length.[60]

### 2.7. Stability experiment

The ambient stability of the modified BPNs was evaluated by measuring the absorbance changes of their water dispersions. BPNs, BPNs@Ag, BPNs@Au, and BPNs@GO (10 mg) were dispersed in DI water (20 mL) and maintained for two different periods of 1 day and 7 days under air and natural light. Their absorbance was recorded after 1 day and 7 days using a UV-vis spectrophotometer.

### 2.8. Dye photodegradation and dye adsorbance studies

Methylene blue (MB) and methyl orange (MO) were selected as the models of cationic and anionic dyes, respectively, for photocatalytic degradation. 10 mg of each sample including RP, bulk BP, BPNs, BPNs@Ag, BPNs@Au, BPNs@GO, and electrospun NFs was placed in 10 mL of dye solution (5 ppm) and stirred slowly under xenon light radiation within 2 h. Then, the solutions were centrifuged and the absorbance spectra of the supernatant were collected at 664 nm for MB and 464 nm for MO. The photodegradation efficiency of the organic dyes over the photocatalytic powders and electrospun NFs was calculated by the following formula:

$$\text{Photodegradation efficiency}(\%) = \left(1 - \frac{C}{C_i}\right) \times 100$$

where $C_i$ is the initial concentration of dye and $C$ is the dye's concentration at different time of light radiation.

The studies in the dark were performed for investigating the dye adsorbance behavior of the photocatalytic powders and electrospun NFs by stirring the solutions in dark within 2 h.

### 2.9. Photodegradation mechanism experiment

To propose the photodegradation mechanism of MO and MB organic dyes, the various radical scavengers of benzoquinone (BQ), tertiary butyl alcohol (TBA), and ethylenediaminetetraacetic acid (EDTA) were used for trapping the species of $O_2^{\bullet-}$, $^{\bullet}OH$, and $h^+$, respectively. The experimental conditions were similar to the photodegradation experiment and the photocatalytic powders and electrospun NFs with the highest photodegradation efficiency (*i.e.* BPNs@GO, BPNs@Ag, BPNs@Au, BPNs@GO-loaded PANi/PAN NFs, BPNs@Ag-loaded PANi/PAN NFs, and BPNs@Au-loaded PANi/PAN NFs) were chosen for the experiment.

## 3. Results and discussion

RP exhibited the FT-IR distinctive peaks related to its intrinsic structure (Fig. 2). Bulk BP and BPNs indicated the absorption peaks at 1050 $cm^{-1}$, 1160 $cm^{-1}$, and ~1620 $cm^{-1}$ corresponded to the stretching modes of P–O, P–P–O, and P=O, respectively.[61] The BPNs@Ag, BPNs@Au, and BPNs@GO did not show any new peaks to confirm the existence of Ag, Au, and GO, so, UV-vis, PXRD, and Raman analyses were further used for confirming the successful modifications. The FT-IR spectra of PANi/PAN NFs and composite NFs are shown in Fig. 2. The peaks at 1566 $cm^{-1}$ and 1480 $cm^{-1}$ are related to stretching vibrations of the benzenoid and quinoid rings (N=Q=N) of PANi and the peaks at 1301 $cm^{-1}$, 1122 $cm^{-1}$, and 805 $cm^{-1}$ are respectively credited to the stretching modes of C–N and N=Q=N and out-of-plane bending of N–H in PANi.[62] PAN displayed the peaks at 2950 $cm^{-1}$ and 1454 $cm^{-1}$ which are related to the stretching and bending vibrations of $-CH_2$ and the peak at 2240 $cm^{-1}$ is attributed to –C≡N. FT-IR spectra of the composite NFs did not show the peaks related to BPNs, BPNs@Ag, BPNs@Au, and BPNs@GO because of the high amount of PANi and PAN polymers as compared to the BP nanosheets.

Decoration of BPNs with Au and Ag NPs was proved by UV-vis spectroscopy with the appearance of maximum absorption peaks at 450 nm and 550 nm, respectively. The results revealed that Au and Ag NPs were successfully produced by the reduction of $Au^{3+}$ and $Ag^+$ ions with BPNs without any additional reductants. The UV-vis spectra of BPNs, GO, and BPNs@GO are shown in Fig. 2. The peak at 230 nm is assigned to π–π* transition of the carboxyl functional group of GO. After modification of BPNs with GO, the characteristic peak at 230 nm is red-shifted to 250 nm which is probably because of the reduction of GO by BPNs.[34] Fig. S5† indicates the reduction of GO by BPNs leading to reduced GO (rGO).

PXRD pattern of RP indicates a sharp reflectance at $2\theta$ = 15.7° which is related to the amorphous nature of RP. After the solvothermal reaction and conversion of RP to BP, the PXRD pattern became completely different from the amorphous RP and no diffraction pattern of RP was observed. Several representative diffraction patterns, which are consistent with the previous literature, were located at 17.0°, 26.7°, 34.3°, 52.5°, 56.2°, and 56.8° corresponding to the (020), (021), (040), (060), (151) and (061) planes of BPNs, respectively[63–65] (Fig. 3). The diffraction pattern of BPNs@Ag displayed the reflectance of Ag at 38.2°, 44.4°, 64.6°, and 77.6° corresponding to (111), (200), (220), and (311) planes, respectively[66,67] and the reflectance of Au were observed at 38.2°, 44.6°, 64.7°, and 77.8° which are attributed to (111), (200), (220), and (222) planes, respectively.[68] The obtained XRD patterns for BPNs@Ag and BPNs@Au indicated that the BPNs were decorated with Au and Ag successfully.

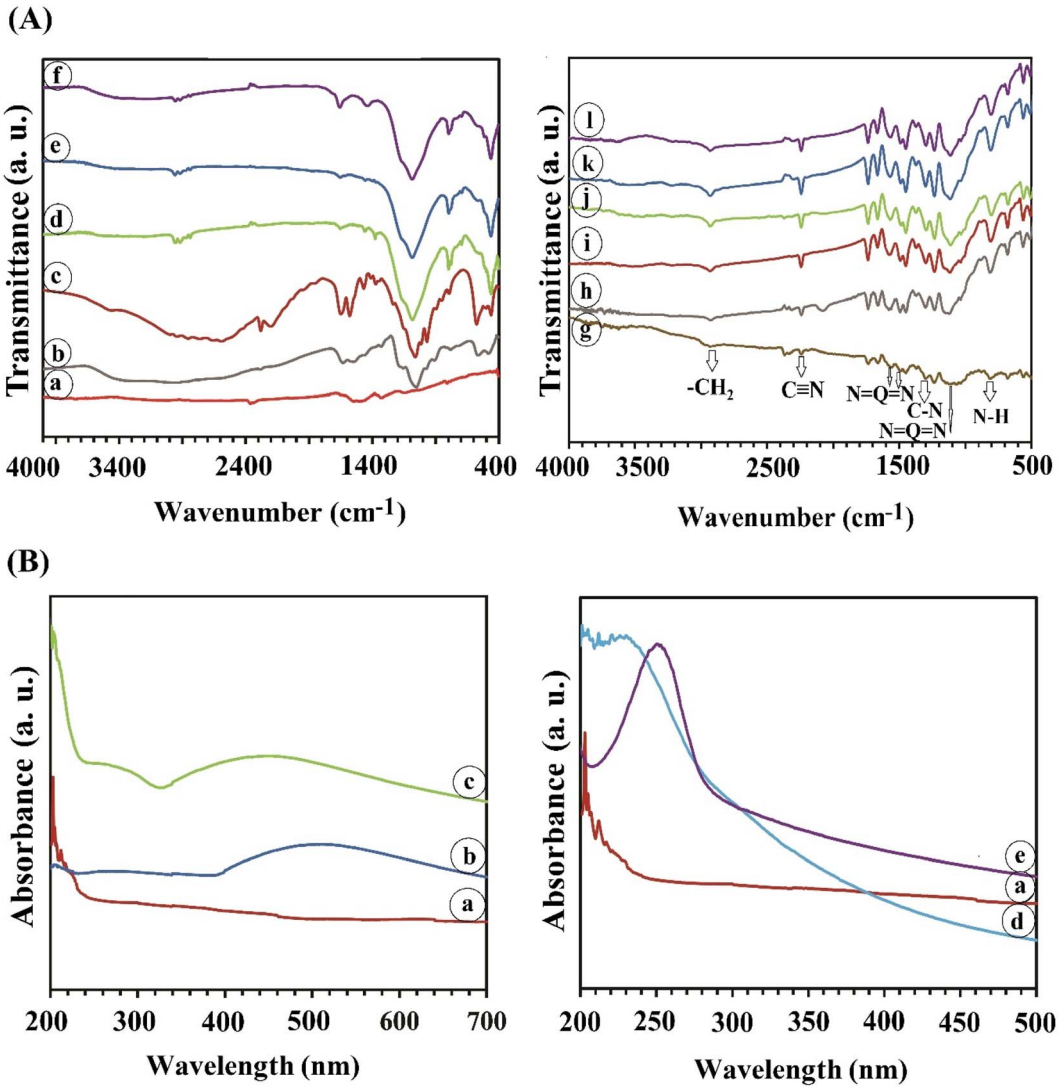


Fig. 2 (A) FT-IR spectra of RP (a), bulk BP (b), BPNs (c), BPNs@Ag (d), BPNs@Au (e), BPNs@GO (f), PANi/PAN NFs (g), bulk BP-loaded PANi/PAN NFs (h), BPNs-loaded PANi/PAN NFs (i), BPNs@Ag-loaded PANi/PAN NFs (j), BPNs@Au-loaded PANi/PAN NFs (k), and BPNs@GO-loaded PANi/PAN NFs (l) and (B) UV-vis spectra of BPNs (a), BPNs@Au (b), BPNs@Ag (c), GO (d), and BPNs@GO (e).

The sharp reflectance of 26.7° related to BPNs is present in the XRD patterns of BPNs@Ag, BPNs@Au, and BPNs@GO. The appeared reflectance around 38° in the XRD patterns of BPNs@Au-loaded PANi/PAN NFs and BPNs@Ag-loaded PANi/PAN NFs is a corroboration for the existence of Au and Ag inside the PANi/PAN NFs. After the modification of BPNs with GO, the oxygen-containing functionalities of GO were reduced by the lone pair electrons of phosphorus atoms in BPNs; thus, the main reflectance of reduced GO appeared at 26.6° which probably has interference with the main reflectance of BPNs at 26.7°. Regarding the XRD patterns, the crystalline structure of BPNs was changed slightly after the decoration with Ag and Au and modification with GO. The PXRD pattern of PANi/PAN NFs indicated a sharp diffraction reflectance at 16.8° attributed to the (100) plane of PAN and showed a broad diffraction pattern at 20°–30° related to PANi with low crystallinity.[69,70] The electrospun composite NFs including BPNs-loaded PANi/PAN NFs, BPNs@Ag-loaded PANi/PAN NFs, BPNs@Au-loaded PANi/PAN NFs, and BPNs@GO-loaded PANi/PAN NFs in addition to showing the reflectance at 20°–30° indicated a sharp diffraction pattern at around 17° related to (020) plane of highly crystalline BP, thus confirming the presence of BP in the electrospun PANi/PAN NFs[71] (Fig. 3).

Raman spectroscopy also affirmed the successful conversion of RP to BPNs (Fig. 3). The Raman spectrum of RP was in agreement with that of the amorphous RP in prior reports,[58,72] where the peaks at 345 $cm^{-1}$, 383 $cm^{-1}$, and 451 $cm^{-1}$ were attributed to $B_1$ (fundamental mode), $A_1$ (symmetric stretch mode), and $E_1$ (degenerate mode) of RP, respectively. The Raman spectrum of bulk BP displayed three peaks at 361 $cm^{-1}$, 437 $cm^{-1}$, and 465 $cm^{-1}$ corresponding to $A_g^1$ (out-of-plane phonon mode), $B_{2g}$ (in-plane mode), and $A_g^2$ (in-plane mode), respectively and no characteristic peak of RP is observed.[73,74] As shown in the Raman spectrum of BPNs, these three prominent

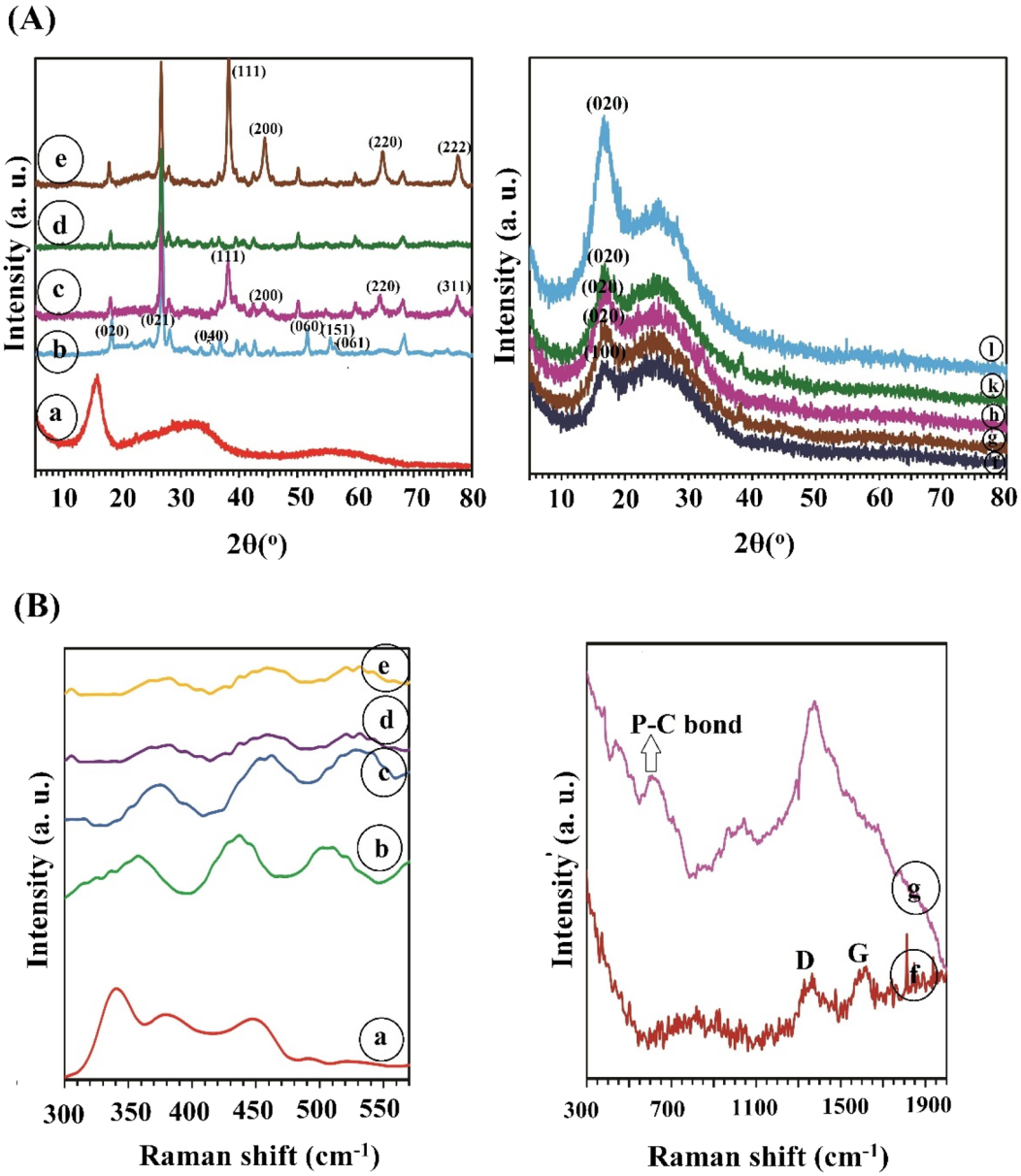


Fig. 3 (A) PXRD patterns of RP (a), BPNs (b), BPNs@Ag (c), BPNs@GO (d), BPNs@Au (e), PANi/PAN NFs (f), BPNs@Au-loaded PANi/PAN NFs (g), BPNs@Ag-loaded PANi/PAN NFs (h), BPNs@GO-loaded PANi/PAN NFs (k), and BPNs-loaded PANi/PAN NFs (l) and (B) Raman spectra of RP (a), bulk BP (b), BPNs (c), BPNs@Ag (d), BPNs@Au (e), GO (f), and BPNs@GO (g).

peaks are slightly blue-shifted when bulk BP is exfoliated to BPNs, which is due to phonon confinement.[75] However, these three Raman peaks are broad that is showing a mixture of nanosheets with variable thicknesses in BPNs.[63] The Raman spectra of BPNs@Au and BPNs@Ag preserved the characteristic peaks of BPNs that is confirming the maintenance of BPNs's structure after decoration with the noble metals of Ag and Au. GO shows a broad D band at 1348 $cm^{-1}$ and a blue-shifted G band at 1610 $cm^{-1}$.[76,77] The blue shifting of the G band can be because of the unmodified graphitic parts.[77] In the Raman spectrum of BPNs@GO, the Raman peaks related to P–P bonds of BPNs in the region 300–500 $cm^{-1}$ show a substantially-decreased intensity because of breaking up the P–P bonds for generation of the P–C bonds. A broad peak at 570–700 $cm^{-1}$ in the Raman spectrum of BPNs@GO is probably for P–C covalent bonding formed between BPNs and GO.[72] The peaks in the range of 1300–1800 $cm^{-1}$ are belonging to GO.

The Raman spectra of PANi, PAN NFs, and PANi/PAN NFs are displayed in Fig. S1.† A broad Raman peak was observed for the PAN NFs. The peak broadness recommends that electrospun PAN NFs have a low crystallinity. The peaks of PANi were distinguished at 1167 $cm^{-1}$, 1506 $cm^{-1}$, 1330 $cm^{-1}$, 1480 $cm^{-1}$, and 1598 $cm^{-1}$ related to C–H bending vibration of the quinoid/benzenoid rings, $C–N^{+}$ vibration of delocalized polaronic structures, N–H deformation vibrations associated with the semi-quinonoid structures, C=N stretching vibrations in

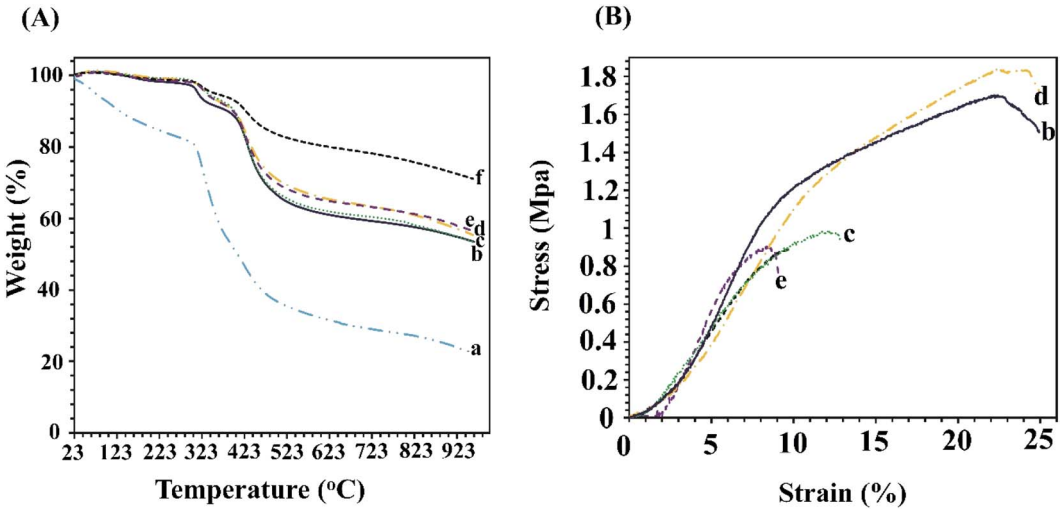


Fig. 4 (A) TGA curves and (B) stress–strain curves of (a) PAN NFs, (b) PANi/PAN NFs, (c) BPNs-loaded PANi/PAN NFs, (d) BPNs@GO-loaded PANi/PAN NFs, (e) BPNs@Ag-loaded PANi/PAN NFs, and (f) BPNs@Au-loaded PANi/PAN NFs.

quinonoid units, and C–C stretching of the benzenoid rings, respectively. The peak at 810 $cm^{-1}$ is attributed to the benzene-ring deformations.[78] These distinctive peaks also appeared in the spectrum of PANi/PAN NFs.

Thermal and mechanical properties of the electrospun composite NFs were investigated by thermogravimetric analysis (TGA) and tensile test, respectively. In TGA curves of NFs (Fig. 4A), the weight loss below 300 °C is due to evaporating the solvent molecules such as water and DMF. The main weight loss detected in the range of 300 °C to 500 °C is for PAN NFs, which is attributed to the thermal decomposition and carbonization of PAN chains. Above 500 °C, another weight loss was determined, indicating the complete transformation of PAN to carbon (complete carbonization).[59] The PANi/PAN NFs exhibited more thermal stability compared to the PAN NFs as they decomposed in two stages (1) the low weight loss at the temperature range of 300–350 °C, which was associated with the removal of the rest of the strongly bound water to PANi as well as due to the presence of low-molecular PANi chains[79] and (2) the weight loss between 390 °C–500 °C which is attributed to PAN cyclization. The final weight loss could be attributed to the carbonation process of the PAN comprising dehydrogenation and denitrogenation processes.[80] After the incorporation of BPNs, BPNs@Ag, BPNs@Au, and BPNs@GO into the PANi/PAN NFs, the second weight loss related to PAN decomposition decreased, as observed in the TGA curves of the composite NFs. For instance, 23% weight loss observed for the PANi/PAN NFs in the temperature range of 390 °C–500 °C decreased to 15% after the incorporation with BPNs@Au.

Table 1 Mechanical properties of the electrospun NFs

| Name | TS (MPa) | EAB (%) |
|---|---|---|
| PANi/PAN NFs | 1.69 | 24.94 |
| BPNs-loaded PANi/PAN NFs | 0.97 | 12.82 |
| BPNs@Ag-loaded PANi/PAN NFs | 0.88 | 9.10 |
| BPNs@Au-loaded PANi/PAN NFs | 0.87 | 9.50 |
| BPNs@GO-loaded PANi/PAN NFs | 1.83 | 24.91 |

The stress–strain curves of the electrospun NFs are shown in Fig. 4B. Table 1 sums up the calculated ultimate tensile strength (TS) and percentage of elongation at break (EAB) for the NFs.

As shown in Fig. 4B, all the NFs exhibited a linear elastic behavior. The incorporation of BPNs, BPNs@Ag, and BPNs@Au into the PANi/PAN NFs could lead to a decrease in the tensile strength of the NFs. It can be probably because of the weak physical interactions between the nanosheets and PANi/PAN matrix and due to the aggregations and non-uniform distribution of BPNs, BPNs@Ag, or BPNs@Au inside the NFs.[81] The minor increase in the TS and decrease in the EAB of the PANi/PAN NFs after the incorporation with BPNs@GO could be attributed to the stronger physical interactions formed between BPNs@GO and PANi/PAN NFs and the inorganic GO part acting as a reinforced material.[82]

The morphology and elemental composition of bulk BP, BPNs, BPNs@Ag, BPNs@Au, and BPNs@GO are shown in Fig. 5. Bulk BP exhibited aggregated and non-uniform particles with rough surfaces while BPNs show typical 2D large sheets with the size of more than 5 μm and a crystalized layered structure. In the SEM images of BPNs@Ag and BPNs@Au, an obvious deposition of aggregated Ag NPs and Au NPs with high coverage could be detected on the surface of BPNs. According to Fig. 5e, the multilayer BP crystals are observed in between the layers of GO sheets, which is further confirmed by the uniform distribution of P and C elements in the mapping of BPNs@GO. The EDAX spectra of bulk BP and BPNs show the element of P which agrees with their elemental dot-mapping images as provided in Fig. S2.† BPNs@Ag and BPNs@Au indicated Ag and Au elements, respectively, as well as P element related to BP. BPNs@GO showed the elements of O and C related to GO and the element of P attributed to BP. The elemental mappings of all the nanosheets are provided in Fig. S2.†

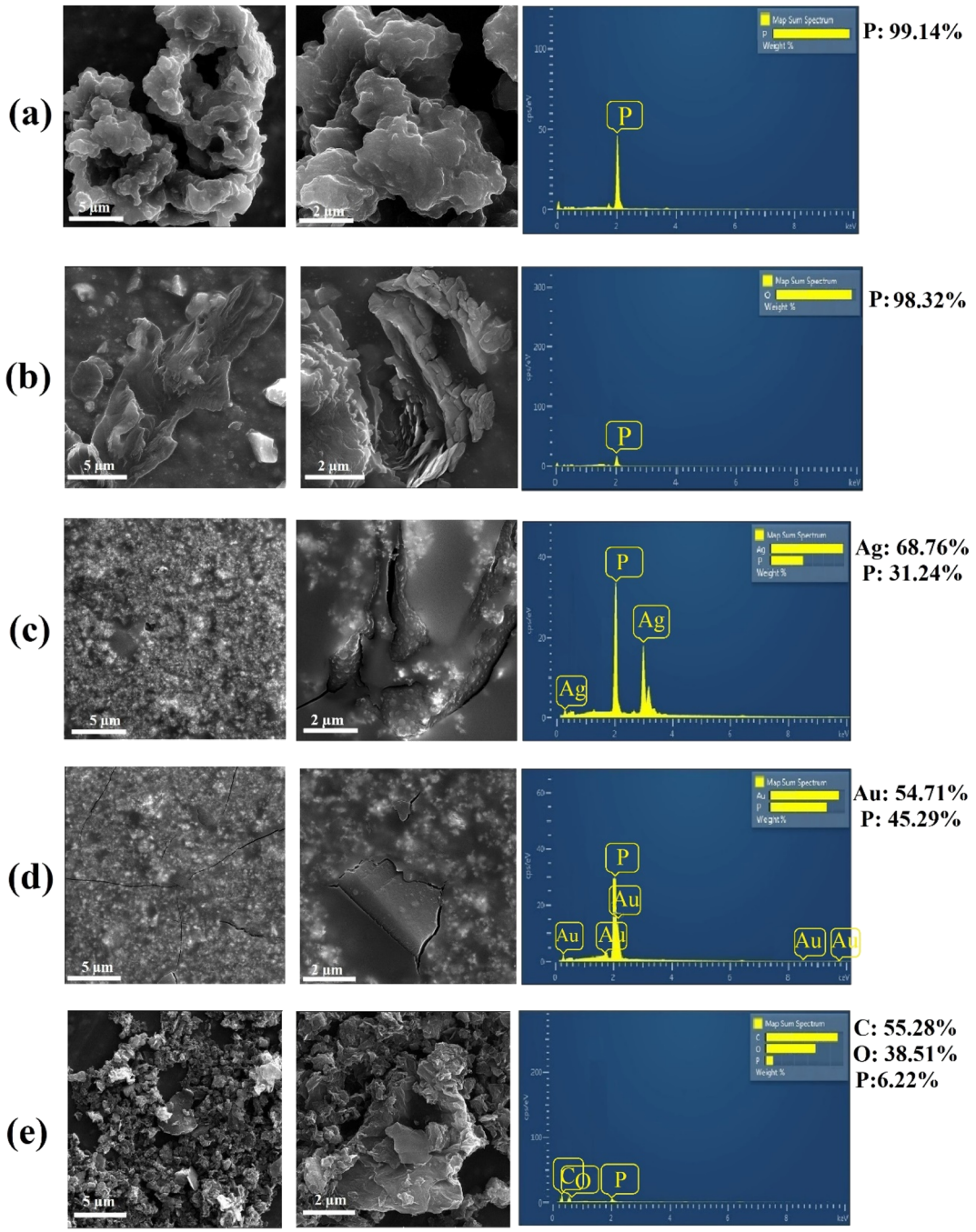


Fig. 5 SEM images and elemental composition of bulk BP (a), BPNs (b), BPNs@Ag (c), BPNs@Au (d), and BPNs@GO (e).

The morphology and elemental composition of the electrospun NFs are presented in Fig. 6. PAN NFs showed a smooth surface and a diameter of 111 nm. The surface of the PAN NFs became rougher after adding the PANi polymer.[62] The PANi/PAN NFs with an average diameter of 130 nm are observed in Fig. 6b. A number of protrusions are observed along the length of PAN/PANi NFs when they are incorporated with BPNs (Fig. 6c), BPNs@Ag (Fig. 6d), BPNs@Au (Fig. 6e), and BPNs@GO (Fig. 6f). These protrusions are individual or clusters of the nanosheets with aggregation.[62] The elemental mapping of all the NFs is provided in Fig. S3.†

The water contact angle measurements were carried out to measure the wettability and hydrophobicity index of the electrospun NFs. This technique provides useful information about the hydrophobicity and hydrophilicity of the surface of materials. A contact angle of less than 90° indicates the high hydrophilicity of the material surface, a contact angle of more than 90° shows a hydrophobic surface, and a water contact angle of greater than 150° indicates a superhydrophobic material. Fig. 7 indicates the contact angles of PAN NFs, PANi/PAN NFs, BPNs-loaded PANi/PAN NFs, BPNs@Ag-loaded PANi/PAN NFs, BPNs@Au-loaded PANi/PAN NFs, and BPNs@GO-

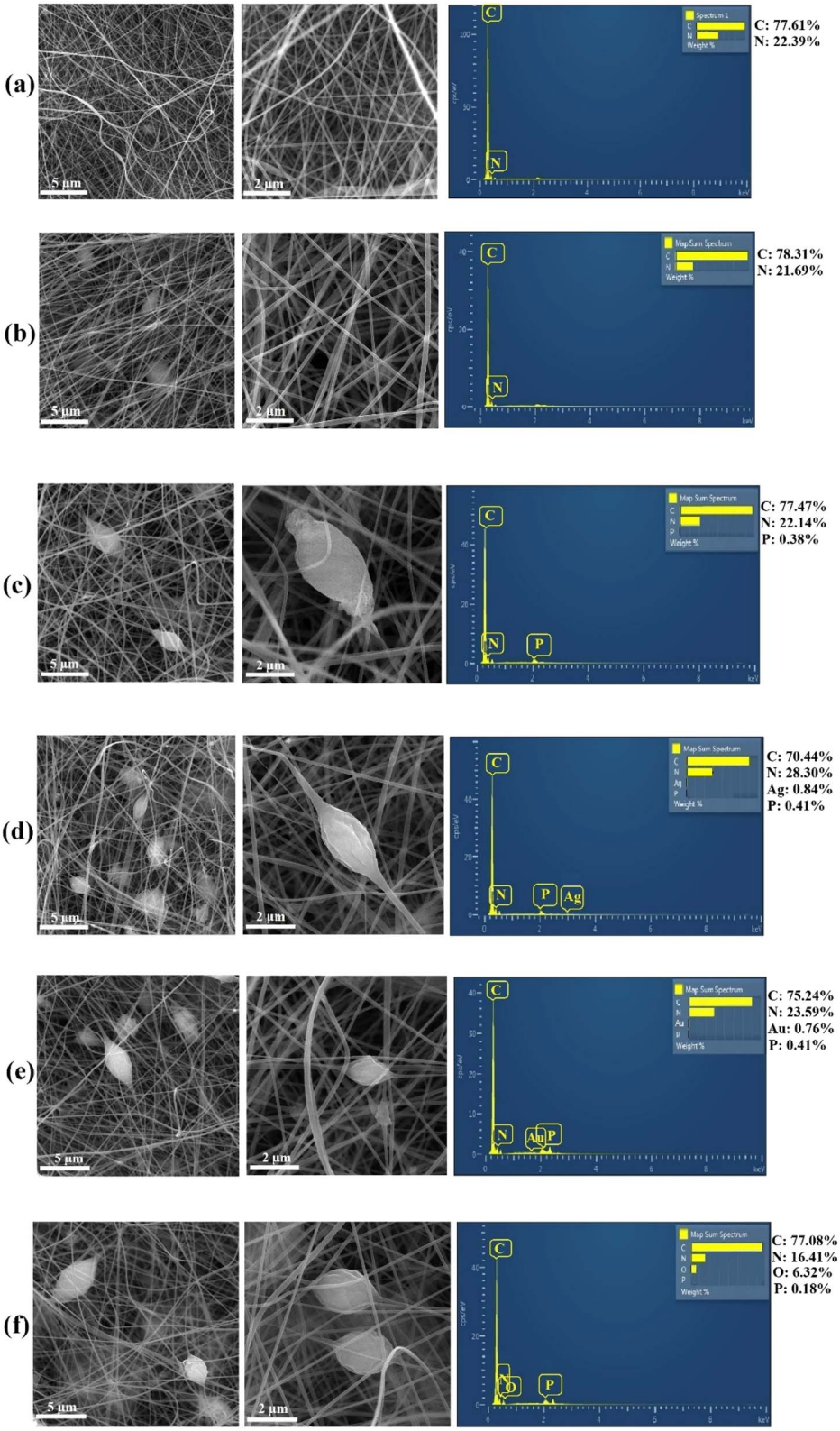


Fig. 6 SEM images and EDAX spectra of PAN NFs (a), PANi/PAN NFs (b), BPNs-loaded PANi/PAN NFs (c), BPNs@Ag-loaded PANi/PAN NFs (d), BPNs@Au-loaded PANi/PAN NFs (e), and BPNs@GO-loaded PANi/PAN NFs (f).

loaded PANi/PAN NFs within a wettability time of zero and droplet amount of 10 μL. All the reported contact angles were less than 90° thus confirming the good hydrophilicity of the NFs. The wettability of PAN NFs increased from 51.29° to 39.28° after combination with PANi which is probably owing to the amine functionalities of PANi polymer. The hydrophilicity

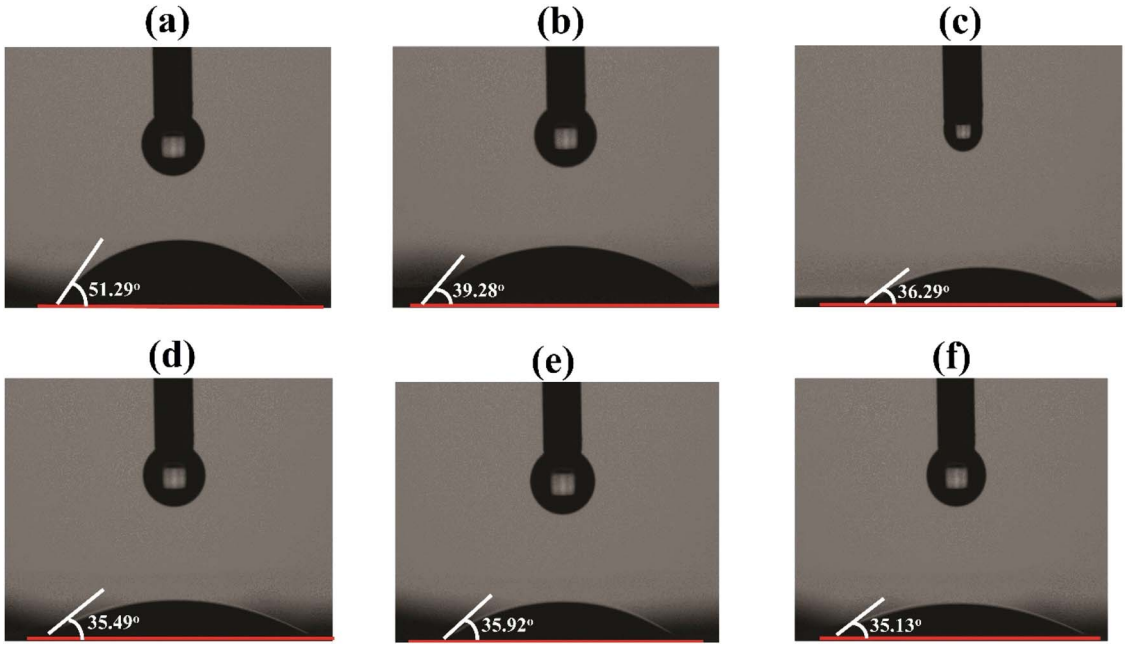


Fig. 7 The water contact angles of PAN NFs (a), PANi/PAN NFs (b), BPNs-loaded PANi/PAN NFs (c), BPNs@Ag-loaded PANi/PAN NFs (d), BPNs@Au-loaded PANi/PAN NFs (e), and BPNs@GO-loaded PANi/PAN NFs (f) within 0 s.

of PANi/PAN NFs increased after incorporation with BPNs, BPNs@Ag, BPNs@Au, and, BPNs@GO. The BPNs@Ag-loaded PANi/PAN NFs, BPNs@Au-loaded PANi/PAN NFs, and BPNs@GO-loaded PANi/PAN NFs indicated the contact angles slightly more than those of the BPNs-loaded PANi/PAN NFs due to the hydroxyl functionalities of Ag and Au NPs and various functional groups of carboxylic acid, hydroxyl, and epoxy groups of GO.[83]

MB (cationic dye) and MO (anionic dye) were selected as the models of organic dyes with a maximum absorbance of MB at 664 nm and MO at 475 nm. The MO and MB photodegradation results over the photocatalytic powders and electrospun NFs are presented in Fig. 8. For the photocatalytic powders, the least MO degradation belongs to RP and the most MO degradation is related to BPNs@GO; MO photodegradation over bulk BP is more than both, for the RP and BPNs. BPNs@Ag and BPNs@Au displayed more degradation of MO dye compared to the BPNs. The results of MB degradation over the photocatalytic powders were approximately similar to the results obtained for MO degradation. The general trend of MO degradation over the photocatalytic powders can be suggested as BPNs@GO (99.6%) > BPNs@Au (98.9%) > BPNs@Ag (95.4%) > BP bulk (25.2%) > BPNs (25.3%) > RP (22.0%) and the general trend of MB degradation over the photocatalytic powders was suggested as BPNs@GO (99.2%) > BPNs@Ag (94.9%) > BPNs@Au (93.1%) > BP bulk (23.3%) > BPNs (20.1%) > RP (18.7%). GO functions as an electron carrier in composites with enhanced catalytic properties. Ag and Au also enhanced the photocatalytic properties of BPNs as they probably function as a sink for electrons on the surface of the photocatalyst leading to interfacial charge transfer and separation of the photogenerated electron–hole pairs.[84]

As observed in Fig. 8, the MO and MB degradation increased with the incorporation of these photocatalytic powders into the PANi/PAN NFs. In other words, the electrospun composite NFs photodegraded the MO and MB dyes more efficiently than the powdered form of photocatalysts and more than the PANi/PAN NFs. Thus, the photocatalytic activity of both PANi/PAN NFs and the powdered form of photocatalysts is enhanced by their combination through the fabrication of electrospun composite NFs. In this way, these composite NFs were not only more effective than the powdered form of the photocatalysts in the degradation of organic dye pollutants but also could reduce the instability and aggregation of the nanoscale photocatalysts,[85] along with their cytotoxicity. In addition, the low density of PAN and the porosity of NFs culminates in simply floating on the surface of the dye solution.[86,87] The good adsorption performance of the NFs provided an advantageous condition for photocatalytic degradation, as dye molecules are adsorbed on the surface of NFs and then migrate to the photocatalyst and eventually degraded.[88] Besides, PANi is a conductive polymer with photocatalytic activity. Polymeric photocatalysts offered several advantages such as chemical inertness, thermal stability, and high surface area.[89,90] The composite NFs displayed more effectiveness on the anionic MO because of the positive zeta potential value of PANi. The photodegradation efficiency over the electrospun NFs were obtained in order of BPNs@GO-loaded PANi/PAN NFs (99.9%) > BP-loaded PANi/PAN NFs (99.3%) > BPNs@Au-loaded PANi/PAN NFs (99.1%) > BPNs@Ag-loaded PANi/PAN NFs (98.1%) > PANi/PAN NFs (97.2%) > BPNs-loaded PANi/PAN NFs (96.0%) > RP-loaded PANi/PAN NFs (60.4%) for MO degradation and in the order of BPNs@GO-loaded PANi/PAN NFs (99.7%) > BPNs@Au-loaded PANi/PAN NFs (98.8%) > BPNs@Ag-loaded PANi/PAN NFs

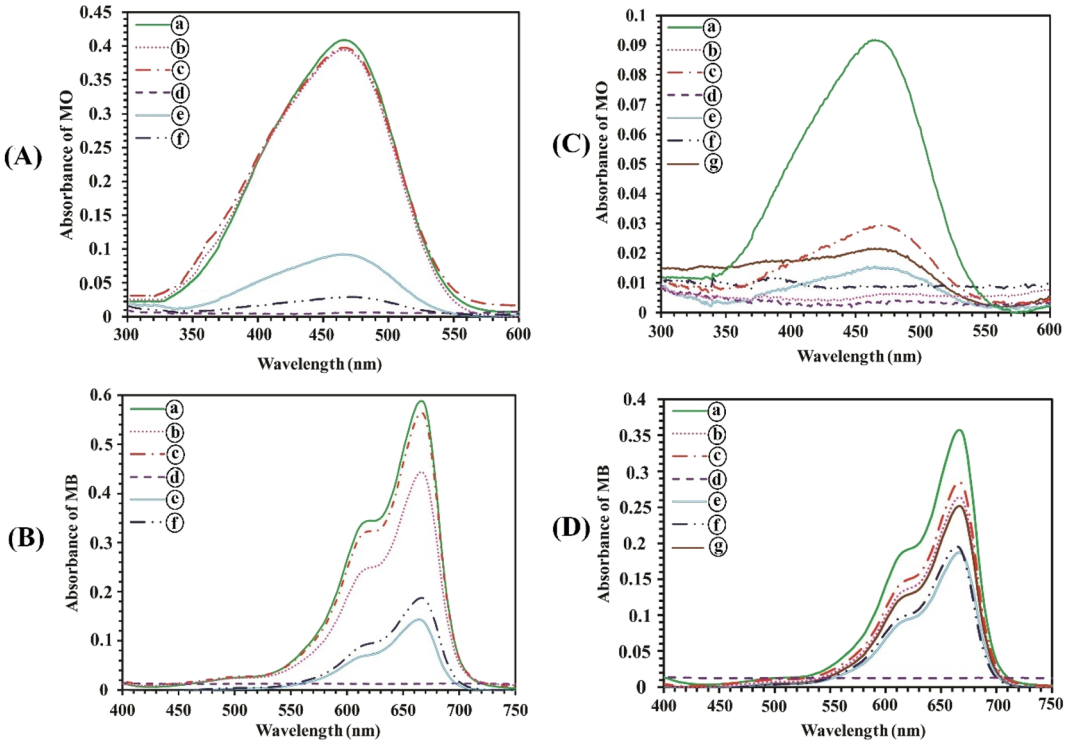


Fig. 8 The photodegradation of MO (A) and MB (B) over the photocatalytic powdered forms of (a) RP, (b) BP bulk, (c) BPNs, (d) BPNs@GO, (e) BPNs@Ag, and (f) BPNs@Au and the photodegradation of MO (C) and MB (D) over the electrospun NFs of (a) RP-loaded PANi/PAN NFs, (b) BP-loaded PANi/PAN NFs, (c) BPNs-loaded PANi/PAN NFs, (d) BPNs@GO-loaded PANi/PAN NFs, (e) BPNs@Ag-loaded PANi/PAN NFs, (f) BPNs@Au-loaded PANi/PAN NFs, and (g) PANi/PAN NFs under light radiation within 2 h.

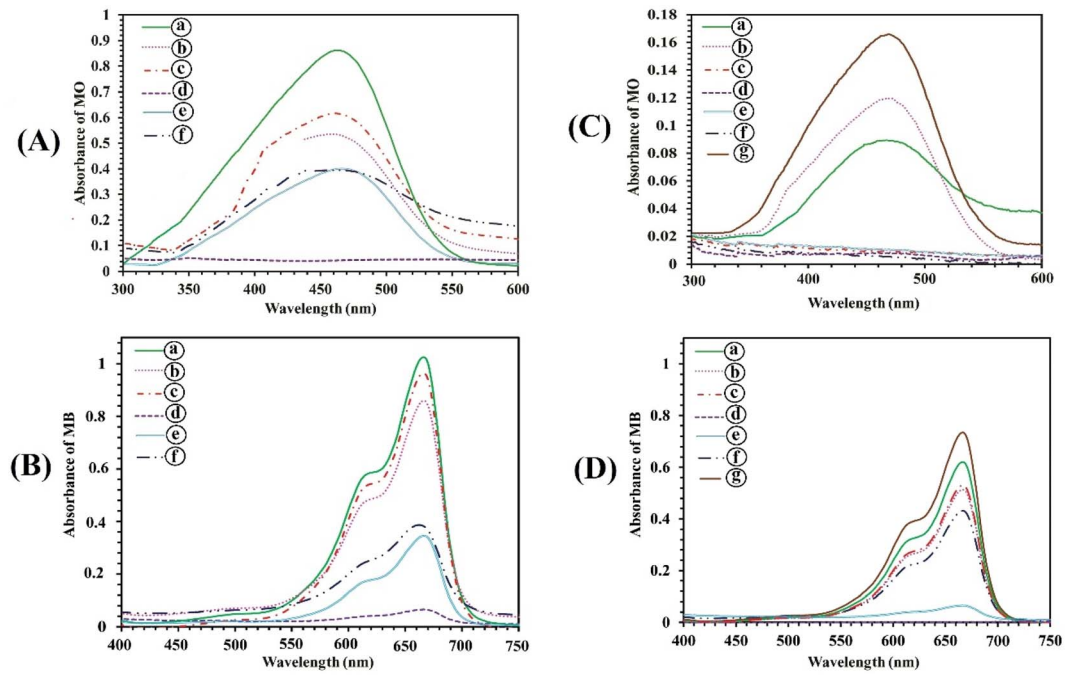


Fig. 9 The adsorbance of MO (A) and MB (B) over the photocatalytic powdered forms of (a) RP, (b) BP bulk, (c) BPNs, (d) BPNs@GO, (e) BPNs@Ag, and (f) BPNs@Au and the adsorbance of MO (C) and MB (D) over the electrospun NFs of (a) RP-loaded PANi/PAN NFs, (b) BP-loaded PANi/PAN NFs, (c) BPNs-loaded PANi/PAN NFs, (d) BPNs@GO-loaded PANi/PAN NFs, (e) BPNs@Ag-loaded PANi/PAN NFs, (f) BPNs@Au-loaded PANi/PAN NFs, and (g) PANi/PAN NFs in the dark within 2 h.

(95.3%) > PANi/PAN NFs (42.1%) > BP-loaded PANi/PAN NFs (40.0%) > BPNs-loaded PANi/PAN NFs (38.3%) > RP-loaded PANi/PAN NFs (34.9%) for MB degradation.

The adsorbance behavior of MO and MB dyes over the photocatalytic powders and electrospun NFs are shown in Fig. 9. Amongst the powders, BPNs@GO revealed the most adsorbance of dyes. The adsorption mechanism of GO is probably through the interactions of π–π, electrostatic, cation–π, and hydrogen bonding.[91] In addition, GO has the potential to adsorb cationic dyes owing to its negative charge, thus expecting to reveal more absorption of MB than MO. As shown, the adsorption of both MO and MB dyes over the electrospun composite NFs was higher than those of the corresponding photocatalytic powders. Also, the NFs prepared through electrospinning had extensive surface area and adsorption active sites making them stronger adsorbents.[92] Also, there is an electrostatic interaction between the PAN and MB. BPNs@Ag-loaded PANi/PAN NFs, BPNs@Au-loaded PANi/PAN NFs, and BPNs@GO-loaded PANi/PAN NFs exhibited more dye adsorbance compared to the PANi/PAN NFs.

The degradation of organic dyes is generally performed by the usual photocatalysis process with the photogenerated electron–hole carriers which produce the main ROS species of $O_2^{\bullet-}$, $^{\bullet}OH$, and $h^+$.[91] According to the results obtained from our photodegradation mechanism's experiment, the $O_2^{\bullet-}$ and $^{\bullet}OH$ species distinguished as the main roles in the MB and MO degradation over all of the chosen photocatalytic powders and electrospun NFs. As shown in Fig. 10, the degradation efficiency of the dyes decreased significantly in the presence of TPA and BQ scavengers in comparision to the EDTA scavenger. In other words, when the $O_2^{\bullet-}$ and $^{\bullet}OH$ species are trapped by their related scavengers, the dye photodegradation decreases. $CO_2$ and $H_2O$ are probably the final products obtained from the degradation of MO and MB dyes by the $O_2^{\bullet-}$ and $^{\bullet}OH$ active species.

BP is unstable and can be oxidized and degraded under ambient conditions when exposed to oxygen and water even without light radiation and produces phosphorus oxide species ($P_xO_y$) and $PO_2^{3-}$, $PO_3^{3-}$, and $PO_4^{3-}$.[9] The ambient stability of BPNs before and after modification with Ag, Au, and GO was investigated within 1 day and 7 days in water under ambient conditions of air and natural light. Fig. S4† indicates the absorbance changes of the water dispersions of BPNs, BPNs@Ag, BPNs@Au, and BPNs@GO. The absorbance intensity of BPNs decreased significantly after 7 days of preserving in water thus confirming the oxidation of BPNs during the time while the difference between the absorbance recorded at 1 day and 7 days was very low for BPNs@Ag, BPNs@Au, and BPNs@GO which reveals the additional ambient stability of these photocatalysts. The improvement in the stability of BPNs@Ag and BPN@Au is probably because of the reaction of $Ag^+$ and $Au^+$ with the P atom on BPNs and occupation of the lone pair of electrons on the P atom to the formation of the

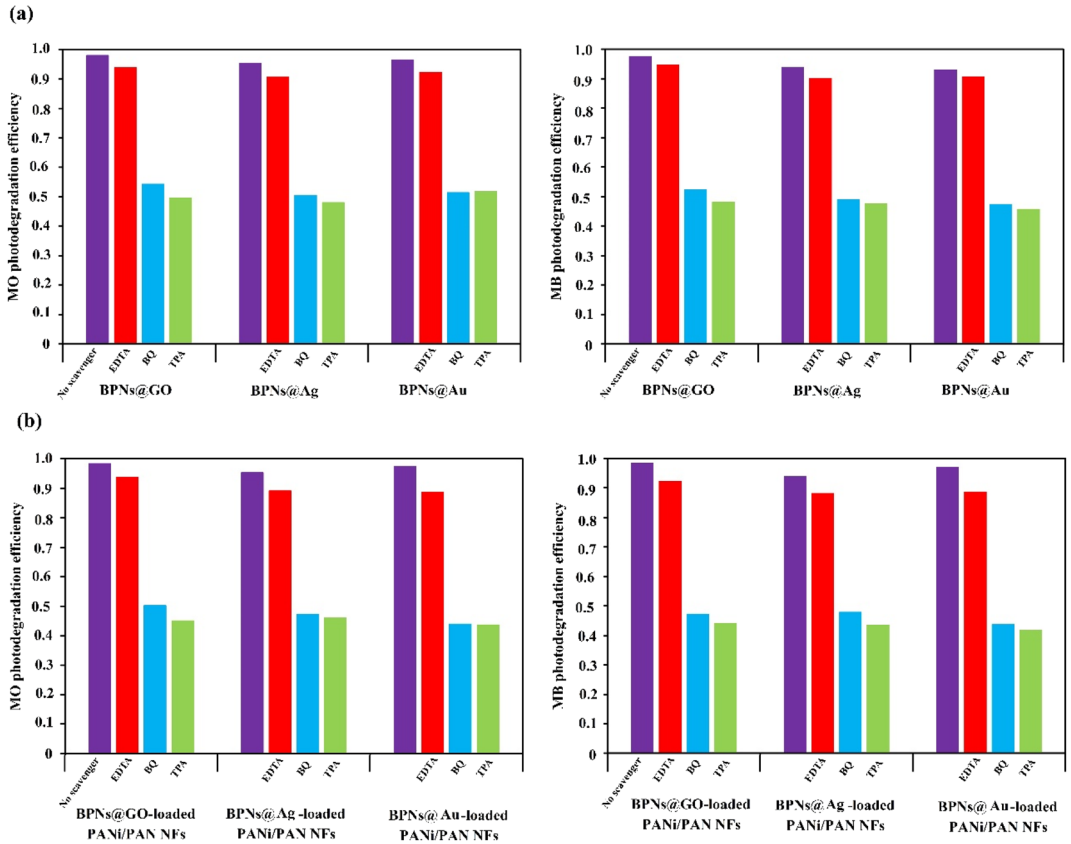


Fig. 10 The photodegradation effect of the photocatalytic powders (a) and electrospun NFs (b) over MB and MO dyes in the absence and existence of scavengers.

stable Ag–P covalent bonds or contact with the surface of BPNs.[30] BP can also reduce the oxygen-containing functional groups of GO and generate P–C and P–O–C covalent bonds.[30,34,35]

## 4. Conclusion

The hydrophilic electrospun composite NFs with enhanced photocatalytic activity were prepared through (1) the modification of BPNs with Ag and Au metals and GO for generating the photocatalytic powders of BPNs@Ag, BPNs@Au, and BPNs@GO and (2) the incorporation of modified BPNs into PANi/PAN NFs by an electrospinning process. The photodegradation of organic dyes over the photocatalytic powdered form of photocatalysts was found in the sequence, BPNs@GO > BPNs@Au > BPNs@Ag > bulk BP $\sim$ BPNs > RP for MO and in the order, BPNs@GO > BPNs@Ag > BPNs@Au > bulk BP > BPNs > RP for MB. The electrospun composite NFs photodegraded the dyes more efficiently than the powdered form of the photocatalysts as well as more effectively than the PANi/PAN NFs. The thermal and mechanical stable composite NFs with enhanced photocatalytic activity can be considered as promising candidates for the elimination of organic dyes from water and wastewater.

## Conflicts of interest

The authors do not have any conflict of interest.

## Acknowledgements

We are grateful for the support of the Research Council of Alzahra University and University of Tehran in this research

## References

1 L. Kou, C. Chen and S. C. Smith, Phosphorene: fabrication, properties, and applications, *J. Phys. Chem. Lett.*, 2015, **6**, 2794–2805.
2 H. Liu, Y. Du, Y. Deng and D. Y. Peide, Semiconducting black phosphorus: synthesis, transport properties and electronic applications, *Chem. Soc. Rev.*, 2015, **44**, 2732–2743.
3 H. Liu, A. T. Neal, Z. Zhu, Z. Luo, X. Xu, D. Tománek and P. D. Ye, Phosphorene: an unexplored 2D semiconductor with a high hole mobility, *ACS Nano*, 2014, **8**, 4033–4041.
4 Z. K. Shen, Y. J. Yuan, P. Wang, W. Bai, L. Pei, S. Wu, Z. T. Yu and Z. Zou, Few-layer black phosphorus nanosheets: a metal-free cocatalyst for photocatalytic nitrogen fixation, *ACS Appl. Mater. Interfaces*, 2020, **12**, 17343–17352.
5 J. Yang, R. Jing, P. Wang, D. Liang, H. Huang, C. Xia, Q. Zhang, A. Liu, Z. Meng and Y. Liu, Black phosphorus nanosheets and ZnAl-LDH nanocomposite as environmental-friendly photocatalysts for the degradation of methylene blue under visible light irradiation, *Appl. Clay Sci.*, 2021, **200**, 105902.
6 E. A. Pogna, A. Bosak, A. Chumakova, V. Milman, B. Winkler, L. Viti and M. S. Vitiello, Lattice dynamics and elastic properties of black phosphorus, *Phys. Rev. B*, 2022, **105**, 184306.
7 L. Cheng, Z. Cai, J. Zhao, F. Wang, M. Lu, L. Deng and W. Cui, Black phosphorus-based 2D materials for bone therapy, *Bioact. Mater.*, 2020, **5**, 1026–1043.
8 R. A. Doganov, E. C. O'farrell, S. P. Koenig, Y. Yeo, A. Ziletti, A. Carvalho, D. K. Campbell, D. F. Coker, K. Watanabe and T. Taniguchi, Transport properties of pristine few-layer black phosphorus by van der Waals passivation in an inert atmosphere, *Nat. Commun.*, 2015, **6**, 6647.
9 T. Zhang, Y. Wan, H. Xie, Y. Mu, P. Du, D. Wang, X. Wu, H. Ji and L. Wan, Degradation chemistry and stabilization of exfoliated few-layer black phosphorus in water, *J. Am. Chem. Soc.*, 2018, **140**, 7561–7567.
10 C. R. Ryder, J. D. Wood, S. A. Wells, Y. Yang, D. Jariwala, T. J. Marks, G. C. Schatz and M. C. Hersam, Covalent functionalization and passivation of exfoliated black phosphorus via aryl diazonium chemistry, *Nat. Chem.*, 2016, **8**, 597–602.
11 V. V. Korolkov, I. G. Timokhin, R. Haubrichs, E. F. Smith, L. Yang, S. Yang, N. R. Champness, M. Schröder and P. H. Beton, Supramolecular networks stabilise and functionalise black phosphorus, *Nat. Commun.*, 2017, **8**, 1385.
12 G. Abellán, V. Lloret, U. Mundloch, M. Marcia, C. Neiss, A. Görling, M. Varela, F. Hauke and A. Hirsch, Noncovalent functionalization of black phosphorus, *Angew. Chem.*, 2016, **128**, 14777–14782.
13 X. Zeng, M. Luo, G. Liu, X. Wang, W. Tao, Y. Lin, X. Ji, L. Nie and L. Mei, Polydopamine-modified black phosphorous nanocapsule with enhanced stability and photothermal performance for tumor multimodal treatments, *Adv. Sci. Lett.*, 2018, **5**, 1800510.
14 G. Zhou, H. Pu, J. Chang, X. Sui, S. Mao and J. Chen, Real-time electronic sensor based on black phosphorus/Au NPs/DTT hybrid structure: application in arsenic detection, *Sens. Actuators, B*, 2018, **257**, 214–219.
15 Z. Guo, S. Chen, Z. Wang, Z. Yang, F. Liu, Y. Xu, J. Wang, Y. Yi, H. Zhang and L. Liao, Metal-ion-modified black phosphorus with enhanced stability and transistor performance, *Adv. Mater.*, 2017, **29**, 1703811.
16 J. Guo, W. Gan, C. Ding, Y. Lu, J. Li, S. Qi, M. Zhang and Z. Sun, Black phosphorus quantum dots and Ag nanoparticles co-modified $TiO_2$ nanorod arrays as powerful photocatalyst for tetracycline hydrochloride degradation: pathways, toxicity assessment, and mechanism insight, *Sep. Purif. Technol.*, 2022, 121454.
17 R. Guan, L. Wang, D. Wang, K. Li, H. Tan, Y. Chen, X. Cheng, Z. Zhao, Q. Shang and Z. Sun, Boosting photocatalytic hydrogen production via enhanced exciton dissociation in black phosphorus quantum Dots/$TiO_2$ heterojunction, *J. Chem. Eng.*, 2022, **435**, 135138.
18 S. Luo, R. Liu, X. Zhang, R. Chen, M. Yan, K. Huang, J. Sun, R. Wang and J. Wang, Mechanism investigation for ultra-efficient photocatalytic water disinfection based on rational design of indirect Z-scheme heterojunction black

phosphorus QDs/$Cu_2O$ nanoparticles, *J. Hazard. Mater.*, 2022, **424**, 127281.
19 P. Ou, X. Zhou, X.-Y. Li, Y. Chen, C. Chen, F. Meng and J. Song, Single-walled black phosphorus nanotube as a $NO_2$ gas sensor, *Mater. Today Commun.*, 2022, **31**, 103434.
20 M. Li, Q. Zhao, S. Zhang, D. Li, H. Li, X. Zhang and B. Xing, Facile passivation of black phosphorus nanosheets via silica coating for stable and efficient solar desalination, *Environ. Sci.: Nano*, 2020, **7**, 414–423.
21 S. Y. Lei, H.-Y. Shen, Y.-Y. Sun, N. Wan, H. Yu and S. Zhang, Enhancing the ambient stability of few-layer black phosphorus by surface modification, *RSC Adv.*, 2018, **8**, 14676–14683.
22 H. Mu, S. Lin, Z. Wang, S. Xiao, P. Li, Y. Chen, H. Zhang, H. Bao, S. P. Lau and C. Pan, Black phosphorus–polymer composites for pulsed lasers, *Adv. Opt. Mater.*, 2015, **3**, 1447–1453.
23 Y. Xu, W. Wang, Y. Ge, H. Guo, X. Zhang, S. Chen, Y. Deng, Z. Lu and H. Zhang, Stabilization of black phosphorous quantum dots in PMMA nanofiber film and broadband nonlinear optics and ultrafast photonics application, *Adv. Funct. Mater.*, 2017, **27**, 1702437.
24 N. Kamyar, R. D. Greenhalgh, T. R. Nascimento, E. S. Medeiros, P. D. Matthews, L. P. Nogueira, H. J. Haugen, D. J. Lewis and J. J. Blaker, Exploiting inherent instability of 2D black phosphorus for controlled phosphate release from blow-spun poly (lactide-co-glycolide) nanofibers, *ACS Appl. Nano Mater.*, 2018, **1**, 4190–4197.
25 J. Zhao, S. C. Nguyen, R. Ye, B. Ye, H. Weller, G. A. Somorjai, A. P. Alivisatos and F. D. Toste, A comparison of photocatalytic activities of gold nanoparticles following plasmonic and interband excitation and a strategy for harnessing interband hot carriers for solution phase photocatalysis, *ACS Cent. Sci.*, 2017, **3**, 482–488.
26 J. Guo, M. Zhang, Z. Yin, C. Ding, P. Chen, W. Gan, H. Yu and Z. Sun, Construction of black phosphorus nanosheets and Ag nanoparticles co-sensitized $TiO_2$ nanorod arrays as high-performance SERS substrate and photocatalyst, *Appl. Surf. Sci.*, 2022, **592**, 153265.
27 S. Moschetto, A. Ienco, G. Manca, M. Serrano-Ruiz, M. Peruzzini, A. Mezzi, M. Brucale, M. Bolognesi and S. Toffanin, Easy and fast in situ functionalization of exfoliated 2D black phosphorus with gold nanoparticles, *Dalton Trans.*, 2021, **50**, 11610–11618.
28 W. Chen, J. Wang, W. Du, J. Wang, L. Cheng, Z. Ge, S. Qiu, W. Pan, L. Song and X. Ma, Black phosphorus nanosheets integrated with gold nanoparticles and polypyrrole for synergistic sonodynamic and photothermal cancer therapy, *ACS Appl. Nano Mater.*, 2021, **4**, 7963–7973.
29 Q. Wu, M. Liang, S. Zhang, X. Liu and F. Wang, Development of functional black phosphorus nanosheets with remarkable catalytic and antibacterial performance, *Nanoscale*, 2018, **10**, 10428–10435.
30 L. Huo, X. Shi and S. Chen, Surface modification and stability performance of black phosphorus nanosheets based on metal ions/graphene, *AIP Adv.*, 2022, **12**, 035150.
31 M. Z. Rahman, C. W. Kwong, K. Davey and S. Z. Qiao, 2D phosphorene as a water splitting photocatalyst: fundamentals to applications, *Energy Environ. Sci.*, 2016, **9**, 709–728.
32 T. Chen, W. Zeng, C. Tie, M. Yu, H. Hao, Y. Deng, Q. Li, H. Zheng, M. Wu and L. Mei, Engineered gold/black phosphorus nanoplatforms with remodeling tumor microenvironment for sonoactivated catalytic tumor theranostics, *Bioact. Mater.*, 2022, **10**, 515–525.
33 L. Li, F. Wang, Y. Liu, F. Cao, B. Zhu and Y. Gu, Local-field-dependent nonlinear optical absorption of black phosphorus nanoflakes hybridized by silver nanoparticles, *J. Phys. Chem. C*, 2021, **125**, 15448–15457.
34 T. Zhou, H. Ni, Y. Wang, C. Wu, H. Zhang, J. Zhang, A. P. Tomsia, L. Jiang and Q. Cheng, Ultratough graphene–black phosphorus films, *Proc. Natl. Acad. Sci. U. S. A.*, 2020, **117**, 8727–8735.
35 A. Avsar, I. J. Vera-Marun, J. Y. Tan, K. Watanabe, T. Taniguchi, A. H. Castro Neto and B. Ozyilmaz, Air-stable transport in graphene-contacted, fully encapsulated ultrathin black phosphorus-based field-effect transistors, *ACS Nano*, 2015, **9**, 4138–4145.
36 F. He, A. Meng, B. Cheng, W. Ho and J. Yu, Enhanced photocatalytic $H_2$-production activity of $WO_3/TiO_2$ step-scheme heterojunction by graphene modification, *Chin. J. Catal.*, 2020, **41**, 9–20.
37 S. P. Lonkar, V. V. Pillai and S. M. Alhassan, Facile and scalable production of heterostructured ZnS–ZnO/graphene nano-photocatalysts for environmental remediation, *Sci. Rep.*, 2018, **8**, 1–14.
38 H. Alwan, K. H. Salem and H. A. Alshamsi, Visible light-driven photocatalytic degradation of Rhodamine B dye onto $TiO_2$/rGO nanocomposites, *Mater. Today Commun.*, 2022, **33**, 104558.
39 J. Yu, J. Li, X. Zhu, X. Zhang, K. Jia, W. Kong, P. Wei, H. Chen, X. Shi and A. M. Asiri, Structured polyaniline: an efficient and durable electrocatalyst for the nitrogen reduction reaction in acidic media, *ChemElectroChem*, 2019, **6**, 2215–2218.
40 F. Köleli and T. Röpke, Electrochemical hydrogenation of dinitrogen to ammonia on a polyaniline electrode, *Appl. Catal., B*, 2006, **62**, 306–310.
41 X. Li, B. Han, Y. Xu, X. Liu, C. Zhao and J. Xu, Conjugated polymer coating enabled light-resistant black phosphorus with enhanced stability, *Nanoscale Adv.*, 2021, **3**, 5650–5655.
42 R. Kumar, J. Travas-Sejdic and L. P. Padhye, Conducting polymers-based photocatalysis for treatment of organic contaminants in water, *J. Chem. Eng. Adv.*, 2020, **4**, 100047.
43 C. Dai and B. Liu, Conjugated polymers for visible-light-driven photocatalysis, *Energy Environ. Sci.*, 2020, **13**, 24–52.
44 K. Namsheer and C. S. Rout, Conducting polymers: a comprehensive review on recent advances in synthesis, properties and applications, *RSC Adv.*, 2021, **11**, 5659–5697.
45 K. Namsheer, S. Kapse, M. Manoj, R. Thapa and C. S. Rout, 2D-black phosphorus/polyaniline hybrids for efficient supercapacitor and hydrogen evolution reaction applications, *Sustainable Energy Fuels*, 2022, **6**, 4285–4298.

46 M. Shanmugam, A. Augustin, S. Mohan, B. Honnappa, C. Chuaicham, S. Rajendran, T. K. Hoang, K. Sasaki and K. Sekar, Conducting polymeric nanocomposites: a review in solar fuel applications, *Fuel*, 2022, **325**, 124899.

47 R. Guo, Y. Jiang, Q. Jia, H. Pei, Z. Mo, N. Liu, X. Niu and Z. Liu, Improved electrocatalytic performance from graphene quantum dots/three-dimensional graphene/polyaniline doped powder to layer-by-layer self-assembled membrane materials, *Mater. Today Commun.*, 2020, **25**, 101426.

48 F. Pierini, M. Lanzi, P. Nakielski and T. A. Kowalewski, Electrospun polyaniline-based composite nanofibers: tuning the electrical conductivity by tailoring the structure of thiol-protected metal nanoparticles, *J. Nanomater.*, 2017, **2017**, 1–10.

49 Z. Q. Feng, X. Yuan and T. Wang, Porous polyacrylonitrile/graphene oxide nanofibers designed for high efficient adsorption of chromium ions (VI) in aqueous solution, *J. Chem. Eng.*, 2020, **392**, 123730.

50 Y. Zhao, H. Wang, H. Huang, Q. Xiao, Y. Xu, Z. Guo, H. Xie, J. Shao, Z. Sun and W. Han, Surface coordination of black phosphorus for robust air and water stability, *Angew. Chem.*, 2016, **128**, 5087–5091.

51 M. Zhou, W. Zou, X. Zhu, H. Ma, P. Wang, J. Shang and P. Luo, In situ growth of UIO-66-$NH_2$ on thermally stabilized electrospun polyacrylonitrile nanofibers for visible-light driven Cr (VI) photocatalytic reduction, *J. Solid State Chem.*, 2022, **307**, 122836.

52 J. Zhan, W. Zhang, M. Wang, W. Guan, X. Yan, Q. Zhang, H. Wang, Z. Wang, Y. Zhang and L. Zou, Fabrication, characterization and antibacterial properties of ZnO nanoparticles decorated electrospun polyacrylonitrile nanofibers membranes, *Mater. Today Commun.*, 2022, **32**, 103958.

53 E. M. Sitinjak, I. Masmur, N. V. M. D. Marbun, P. E. Hutajulu, G. Gultom and Y. Sitanggang, Direct Z-scheme of n-type CuS/p-type ZnS@electrospun PVP nanofiber for the highly efficient catalytic reduction of 4-nitrophenol and mixed dyes, *RSC Adv.*, 2022, **20512**, 16165–16173.

54 X. Li, Q. Wu, M. Hussain, L. Chen, Q. Huang, W. Huang and T. Tao, Sodium alkoxide-mediated $gC_3N_4$ immobilized on a composite nanofibrous membrane for preferable photocatalytic activity, *RSC Adv.*, 2022, **12**, 15378–15384.

55 A. Moheman, M. S. Alam, A. Gupta, S. Dhakate, A. Kumar and A. Mohammad, Fabrication of nanofiber stationary phases from chopped polyacrylonitrile co-polymer microfibers for use in ultrathin layer chromatography of amino acids, *RSC Adv.*, 2016, **6**, 90100–90110.

56 A. Gupta, N. Khosla, V. Govindasamy, A. Saini, K. Annapurna and S. Dhakate, Trimetallic composite nanofibers for antibacterial and photocatalytic dye degradation of mixed dye water, *Appl. Nanosci.*, 2020, **10**, 4191–4205.

57 S. Zhu, Q. Liang, Y. Xu, H. Fu and X. Xiao, Facile Solvothermal synthesis of black phosphorus nanosheets from red phosphorus for efficient photocatalytic hydrogen evolution, *Eur. J. Inorg. Chem.*, 2020, **2020**, 773–779.

58 A. Ozawa, M. Yamamoto, T. Tanabe, S. Hosokawa and T. Yoshida, Black phosphorus synthesized by solvothermal reaction from red phosphorus and its catalytic activity for water splitting, *J. Mater. Chem. A*, 2020, **8**, 7368–7376.

59 D. Li, D. Wang, K. Rui, Z. Ma, L. Xie, J. Liu, Y. Zhang, R. Chen, Y. Yan and H. Lin, Flexible phosphorus doped carbon nanosheets/nanofibers: electrospun preparation and enhanced Li-storage properties as free-standing anodes for lithium ion batteries, *J. Power Sources*, 2018, **384**, 27–33.

60 S. Asgari, G. M. Ziarani, A. Badiei, M. Setayeshmehr, M. Kiani and A. Pourjavadi, Electrospun Ag-decorated reduced GO-graft-chitosan composite nanofibers with visible light photocatalytic activity for antibacterial performance, *Chemosphere*, 2022, **299**, 134436.

61 G. Yang, X. Wan, Z. Gu, X. Zeng and J. Tang, Near infrared photothermal-responsive poly (vinyl alcohol)/black phosphorus composite hydrogels with excellent on-demand drug release capacity, *J. Mater. Chem. B*, 2018, **6**, 1622–1632.

62 L. Tang, J. Dai, Y. T. Liu, Z. L. Li, T. F. Yi, L. Cai, J. Yu and B. Ding, Black phosphorus quantum dots supported by a conductive polymer nanofibrous membrane: a self-standing, metal-free electrocatalyst for nitrogen fixation, *Compos. Commun.*, 2021, **23**, 100551.

63 X. Zhu, T. Zhang, Z. Sun, H. Chen, J. Guan, X. Chen, H. Ji, P. Du and S. Yang, Black phosphorus revisited: a missing metal-free elemental photocatalyst for visible light hydrogen evolution, *Adv. Mater.*, 2017, **29**, 1605776.

64 J. Wang, J. Wang, S. Qiu, W. Chen, L. Cheng, W. Du, J. Wang, L. Han, L. Song and Y. Hu, Biodegradable L-lysine-modified amino black phosphorus/poly (l-lactide-coε-caprolactone) nanofibers with enhancements in hydrophilicity, shape recovery and osteodifferentiation properties, *Colloids Surf., B*, 2022, **209**, 112209.

65 H. Z. Lin and Y. J. Lin, Incorporation of black phosphorus into poly (3-hexylthiophene)/n-type Si devices resulting improvement in rectifying and optoelectronic performances, *Synth. Met.*, 2016, **220**, 538–542.

66 S. S. Shankar, A. Ahmad and M. Sastry, Geranium leaf assisted biosynthesis of silver nanoparticles, *Biotechnol. Prog.*, 2003, **19**, 1627–1631.

67 J. Huang, Q. Li, D. Sun, Y. Lu, Y. Su, X. Yang, H. Wang, Y. Wang, W. Shao and N. He, Biosynthesis of silver and gold nanoparticles by novel sundried cinnamomum camphora leaf, *Nanotechnology*, 2007, **18**, 105104.

68 K. Ma, Y. Cheng, X. Wei, D. Chen, X. Zhao and P. Jia, Gold embedded chitosan nanoparticles with cell membrane mimetic polymer coating for pH-sensitive controlled drug release and cellular fluorescence imaging, *J. Biomater. Appl.*, 2021, **35**, 857–868.

69 Z. Huang, L. Li, Y. Wang, C. Zhang and T. Liu, Polyaniline/graphene nanocomposites towards high-performance supercapacitors: a review, *Compos. Commun.*, 2018, **8**, 83–91.

70 H. G. Chae, T. Sreekumar, T. Uchida and S. Kumar, A comparison of reinforcement efficiency of various types of

 

carbon nanotubes in polyacrylonitrile fiber, *Polymer*, 2005, **46**, 10925–10935.

71 C. Wang, J. Gao, J. G. Zhao, D. J. Yan and X. D. Zhu, Synergistically coupling black phosphorus quantum dots with $MnO_2$ nanosheets for efficient electrochemical nitrogen reduction under ambient conditions, *Small*, 2020, **16**, 1907091.

72 J. Sun, G. Zheng, H.-W. Lee, N. Liu, H. Wang, H. Yao, W. Yang and Y. Cui, Formation of stable phosphorus–carbon bond for enhanced performance in black phosphorus nanoparticle–graphite composite battery anodes, *Nano Lett.*, 2014, **14**, 4573–4580.

73 H. B. Ribeiro, M. A. Pimenta and C. J. de Matos, Raman spectroscopy in black phosphorus, *J. Raman Spectrosc.*, 2018, **49**, 76–90.

74 S. Liang, M. N. Hasan and J.-H. Seo, Direct observation of Raman spectra in black phosphorus under uniaxial strain conditions, *Nanomaterials*, 2019, **9**, 566.

75 X. Du, J. Qiu, S. Deng, Z. Du, X. Cheng and H. Wang, Flame-retardant and form-stable phase change composites based on black phosphorus nanosheets/cellulose nanofiber aerogels with extremely high energy storage density and superior solar-thermal conversion efficiency, *J. Mater. Chem. A*, 2020, **8**, 14126–14134.

76 K. Satheesh and R. Jayavel, Synthesis and electrochemical properties of reduced graphene oxide via chemical reduction using thiourea as a reducing agent, *Mater. Lett.*, 2013, **113**, 5–8.

77 K. N. Kudin, B. Ozbas, H. C. Schniepp, R. K. Prud'Homme, I. A. Aksay and R. Car, Raman spectra of graphite oxide and functionalized graphene sheets, *Nano Lett.*, 2008, **8**, 36–41.

78 J. Stejskal, M. Trchová, P. Bober, P. Humpolíček, V. Kašpárková, I. Sapurina, M. A. Shishov, and M. Varga, *Conducting Polymers: Polyaniline, Encyclopedia of Polymer Science and Technology*, 2015, vol. 2002, pp. 1–44.

79 H. Zeghioud, S. Lamouri, Y. Mahmoud and T. Hadj-Ali, Preparation and characterization of a new polyaniline salt with good conductivity and great solubility in dimethyl sulfoxyde, *J. Serb. Chem. Soc.*, 2015, **80**, 1435–1448.

80 L. Zhang, J. Luo, T. J. Menkhaus, H. Varadaraju, Y. Sun and H. Fong, Antimicrobial nano-fibrous membranes developed from electrospun polyacrylonitrile nanofibers, *J. Membr. Sci.*, 2011, **369**, 499–505.

81 S. Asgari, A. Pourjavadi, M. Setayeshmehr, A. Boisen and F. Ajalloueian, Encapsulation of drug-loaded graphene oxide-based nanocarrier into electrospun pullulan nanofibers for potential local chemotherapy of breast cancer, *Macromol. Chem. Phys.*, 2021, **222**, 2100096.

82 S. Chand, Review carbon fibers for composites, *J. Mater. Sci.*, 2000, **35**, 1303–1313.

83 J. Hou, J. Yun, W. Jang, J. H. Kim and H. Byun, Polyacrylonitrile nanofiber membranes incorporated with large reduced graphene oxide content in situ, *J. Mater. Sci.*, 2021, **56**, 18508–18521.

84 L. Wang, J. Ali, C. Zhang, G. Mailhot and G. Pan, Simultaneously enhanced photocatalytic and antibacterial activities of $TiO_2$/Ag composite nanofibers for wastewater purification, *J. Environ. Chem. Eng.*, 2020, **8**, 102104.

85 H. Wang, M. Zhang, X. He, T. Du, Y. Wang, Y. Li and T. Hao, Facile prepared ball-like $TiO_2$ at GO composites for oxytetracycline removal under solar and visible lights, *Water Res.*, 2019, **160**, 197–205.

86 A. P. Shah, S. Jain, V. J. Mokale and N. G. Shimpi, High performance visible light photocatalysis of electrospun PAN/ZnO hybrid nanofibers, *J. Ind. Eng. Chem.*, 2019, **77**, 154–163.

87 Y. Shi, D. Yang, Y. Li, J. Qu and Z.-Z. Yu, Fabrication of PAN@$TiO_2$/Ag nanofibrous membrane with high visible light response and satisfactory recyclability for dye photocatalytic degradation, *Appl. Surf. Sci.*, 2017, **426**, 622–629.

88 C. Prahsarn, W. Klinsukhon and N. Roungpaisan, Electrospinning of PAN/DMF/$H_2O$ containing $TiO_2$ and photocatalytic activity of their webs, *Mater. Lett.*, 2011, **65**, 2498–2501.

89 V. S. Vyas and B. V. Lotsch, Organic polymers form fuel from water, *Nature*, 2015, **521**, 41–42.

90 S. Kumar, M. Y. Wani, C. T. Arranja, J. A. e Silva, B. Avula and A. J. Sobral, Porphyrins as nanoreactors in the carbon dioxide capture and conversion: a review, *J. Mater. Chem. A*, 2015, **3**, 19615–19637.

91 K. Varaprasad, T. Jayaramudu and E. R. Sadiku, Removal of dye by carboxymethyl cellulose, acrylamide and graphene oxide via a free radical polymerization process, *Carbohydr. Polym.*, 2017, **164**, 186–194.

92 A. Abd-Elhamid, M. El-Aassar, G. F. El Fawal and H. M. Soliman, Fabrication of polyacrylonitrile/β-cyclodextrin/graphene oxide nanofibers composite as an efficient adsorbent for cationic dye, *Environ. Nanotechnol., Monit. Manage.*, 2019, **11**, 100207.